RSC Advances

ROYAL SOCIETY OF CHEMISTRY

www.rsc.org/advances

Cite this: DOI: 10.1039/c0xx00000x

www.rsc.org/xxxxxx

PAPER

Dual roles of iron powder on the synthesis of $LiFePO_4$@C/graphene cathode nanocomposite for high-performance lithium ion batteries

Tiefeng Liu[ab], Jingxia Qiu[b], Bo Wang[a], Yazhou Wang[b], Dianlong Wang*[a] and Shanqing Zhang*[b]

Received (in XXX, XXX) Xth XXXXXXXXX 20XX, Accepted Xth XXXXXXXXX 20XX

DOI: 10.1039/b000000x

Robust, conductive, and cost-effective $LiFePO_4$@C/graphene composites are critical in the production of high performance $LiFePO_4$ lithium ion batteries. Herein, a facile method is designed to synthesize $LiFePO_4$@C/graphene nanocomposite by utilizing low-cost iron powder, wherein the iron powder offers dual roles: the raw source for $LiFePO_4$ and the green reductant for graphene oxide (GO). In this proposed process, GO is reduced to reduced graphene oxide (rGO) by the iron powder and the produced iron ions are adsorbed on the surface of rGO. As a precursor of $LiFePO_4$, the adsorbed iron ions facilitate the formation and the strong and uniform anchoring of the $LiFePO_4$ nanoparticles onto the rGO surface. The resultant robust structure could prevent the rGO from restacking, help maintain the integrity of $LiFePO_4$@C/graphene nanocomposite and afford electronic and ionic conductivity in the rapid charge/discharge process. Consequently, the as-prepared nanocomposite exhibits an excellent high-rate capability and outstanding cycling stability. A discharge capacity of *ca.* 131 mAh•g^{-1} is obtained at 5 *C* rate and a remarkable cycling stability of capacity retention up to 95% is achieved over 1000 cycles.

Introduction

Lithium ion batteries (LIBs) are bound to achieve the large-scale application in the field of (hybrid) electric vehicles and smart grids.[1] Cost, safety, lifespan, energy density and power performance are commonly considered as the major criteria for the proper electrode materials for LIBs.[2-4] Olivine $LiFePO_4$ (LFP) is regarded as a promising cathode due to its natural advantages: reasonable theoretical capacity of 170 mAh•g^{-1}, good durability, natural abundance and relative safety in the fully charge state.[5, 6] However, those requirements cannot always be met by a single electrode material without any modifications. The low ionic and electronic conductivity of LFP results in inferior electrochemical performance at high power density. In this regard, enormous efforts have been devoted to overcome these drawbacks by coating electronic conductive materials and tailoring the morphology.[7-16] Carbonaceous materials are considered as the best option because they have high electronic conductivity, low-cost and environmentally friendliness.[17-19] Simultaneously, both particle growth and aggregation are effectively inhibited. In particular, two-dimensional graphene is highly conductive with an extremely large surface area.[20-24] It is an ideal material for carbon-coated LFP nanoparticles to assure satisfactory electronic conductivity of the composite.

Although high quality LFP/graphene nanocomposites with excellent electronic conductivity and ionic mass transport capability have been reported for LIBs,[25-27] achieving impressive rate performance and cycling life, these processes commonly demand the use of expensive precursors, such as ferrous salts[28, 29] and defect-free graphene,[30] and the expensive chemical equipment, such as high pressure reactor[31, 32] and chemical vapour deposition,[33] using critical reaction conditions such as high vacuum, high temperature and sophisticated reaction procedures.[34] Manufacturing strategies with low raw material cost and production by low energy consumption, minimum by-products and low facility requirements potentially advance the mass production of LFP/graphene composites. To address these challenges in balancing rate performance and production cost, it would be ideal if a synthesis solution could effectively reduce the raw materials cost of LFP/graphene, and simultaneously relegate the production cost via reducing reaction steps and production process.

Generally, graphene oxide (GO) is selected as the precursor of graphene due to its low cost and good dispersion in aqueous solution.[35] The GO are commonly reduced to graphene *via* chemical processes using reductants, such as such as N_2H_4, $NaBH_4$ and HI.[24, 36, 37] These reductants are not only expensive but also toxic. Furthermore, the restacking of the graphene sheets could downgrade the superior surface area of the graphene. Additionally, the bonding strength between LFP grains and graphene is crucial to the lifespan of the composites, especially under high-rate current density. Although there is only 6.8% change in volume upon the Li^+ insertion/desertion,[38] the frequent shrinking and swelling processes potentially result in the fracture and loss of electrical contact[11, 39]. It was well recognized that the pre-adsorption of the metal ions precursors onto the graphene sheets is beneficial in establishing strong bonding between the electrode materials (such as Co_3O_4, TiO_2 and SnO_2) and

graphene.[40-43] The resultant nanoparticles facilitate the even distribution of graphene sheets in the nanocomposites and prevent the graphene sheets from restacking.[44]

In this work, low-cost iron powder is selected to reduce GO and act as the LFP precursor. In the design, GO is firstly reduced by the iron powder in the present of oxalic acid (OA). Simultaneously, iron ions are produced and strongly adsorbed on the fresh rGO surface. More importantly, these adsorbed iron ions are regarded as the prior LFP nuclei. Along with the addition of $NH_4H_2PO_4$, $LiNO_3$ and sugar, the iron ions attached on the rGO surface can be subjected to a carbothermal reaction and converted to LFP nanoparticles that are cemented into three-dimensional graphene structure with *in-situ* formed carbon coating. These two-stage of chemical and thermal reaction processes to GO is beneficial to both the electronic and ionic conductivity of the composite. Finally, a robust nanocomposite consisting of large amount of carbon-coated LFP nanograins strongly and uniformly anchored on a high-conductive graphene sheet is prepared, which is noted as LFP@C/Fe-rGO. Systematic material characterizations are conducted to investigate the properties of the resultant nanocomposite such as its crystalline phase, surface area and porosity. Given the fact that a series of measures are adopted to achieve high surface area, the electronic conductivity, uniform dispersion and strong mechanical bindings of the LFP@C/Fe-rGO, the resultant cathode composite is expected to deliver excellent electrochemical performance in term of rate capacity and capacity retention.

Experimental

Materials preparation

0.158 g GO (using a modified Hummer's method [45]) was dispersed in distilled water by the sonication for 1 h. 1.12 g Iron powder and 2.52 g OA is added into the above solution by order, which was allowed to stand for 1 h in the water bath at 80 °C. Subsequently, the excess HNO_3 was added into the solution in order to dissolve the residual iron powder and oxidize the Fe^{2+} ions to Fe^{3+} ions. Meanwhile, 2.3 g $NH_4H_2PO_4$ (AR) and 1.45 g $LiNO_3$ (AR) was weighed out according to the molar ratio of Fe:P:Li =1:1:1.05 and dissolved in distilled water. 1.9 g sucrose (the weight ratio of sucrose to $LiFePO_4$ was 6:10) was added into the above solution as a carbon source for carbon coating and the reduction of Fe^{3+} to Fe^{2+} during subsequent calcination process. The mixed solution was heated at 80 °C with continuous stirring in air to evaporate excess water, followed by obtaining a homogeneous rheological body. The rheological body was dried at 100 °C and heat-treated at 260 °C for 2 h under Ar atmosphere for the decomposition of nitrate and sucrose pyrolysis. The obtained bulk precursor was treated with high energy ball milling in a hardened steel vial with zirconia balls in ethanol using 01-HD/HDDM Lab Attritor at 1500 rpm for 30 minutes and dried to remove ethanol. Finally, the nano-sized precursor was sintered through a carbothermal reduction process at 650 °C for 9 h under Ar atmosphere. Therefore, a carbon-coated $LiFePO_4$/graphene nanocomposite was prepared, which was denoted as LFP@C/Fe-rGO. Meanwhile, two comparative samples were prepared with directly using GO and thermal-reduced GO with the identical method, which was denoted as LFP@C/GO and LFP@C/T-rGO, respectively.

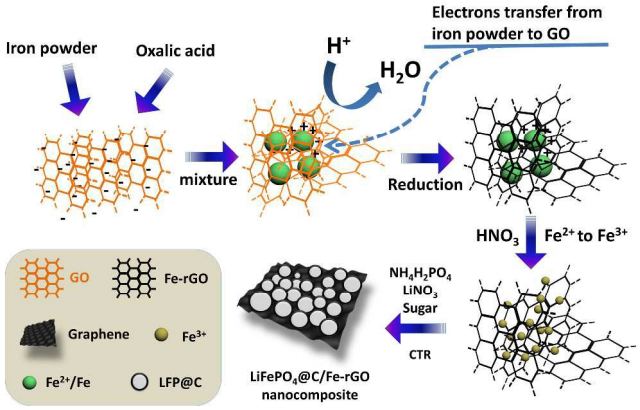

Fig. 1. The schematic illustration of the synthesis route of LFP@C/Fe-rGO nanocomposite.

Physical characterization

X-ray diffraction (XRD) patterns of the as-prepared materials were collected on a D/max-γB X-ray diffractometer (Rigaku, Japan) using Cu Kα radiation (λ=1.54178). The diffraction angle was scanned from 10° to 60° at the scanning speed of 0.02 $°s^{-1}$. The morphology and microstructure of the as-prepared materials were characterized by field-emission scanning electron microscopy (SU8000 Series) and high resolution transmission electron microscopy (JEM-2100). Kratos Axis ULTRA X-ray photoelectron spectrometer (XPS) incorporating a 165 nm hemispherical electron-energy analyser and Brunauer–Emmett–Teller (BET, Micromeritics TriStar II surface area and porosity analyser) measurements were used. The carbon content of the composite was measured by thermo-gravimetric (TG) on an STA449F3 (NETSCH, Germany).

Electrochemical tests

The electrochemical performances of as-prepared materials were evaluated by using a CR2025 coin-type cell. Active materials (80 wt.%), acetylene black (10 wt.%), and a polyvinylidene fluoride (PVDF) binder (10 wt.%) were dispersed in N-methylpyrrolidone (NMP) solvent to form a homogeneous slurry. The obtained slurry was plastered on an Al foil and then dried at 100 °C overnight in a vacuum oven. The working electrode was fabricated by cutting round disks of 14 mm in diameter. The average mass loading of the as-obtained electrodes is 1.36 mg. The coin-type cell was assembled with a Li foil as the counter electrode, a polypropylene micro-porous film (Celgard 2400) as separator, and EC/DMC/DEC-based (1:1:1 by weight) organic solvents containing 1 M of $LiPF_6$ as electrolyte. Galvanostatic charge–discharge tests were investigated by using Neware Battery Testing System at different rates with a voltage window of 2.5~4.2 V (*vs.* Li^+/Li). All the charge procedures were performed at constant current and following constant voltage within 10 minutes. Cyclic voltammetry (CV) measurements (2.5~4.2 V, 0.1 $mV·s^{-1}$) were performed on CHI 630B electrochemical workstation. All the tests were performed at room temperature (23 °C) and all the capacities in this article are based on the mass of as-prepared composites.

Results and discussion

Characterization of electrode materials

According to our design, GO is firstly reduced by iron powder in the presence of oxalic acid. After the addition of iron powder and oxalic acid into the GO solution, the solution is stirred for 5 min and placed in the water bath for 1h. It is observed that a colour change from brown of GO to black of Fe-rGO in Fig. 2a, indicating the GO reduction. However, only using Fe powder cannot reduce the GO to rGO without the assistance of the acid. [36, 46] It is explained that GO can easily capture hydrions from carboxyl groups of OA to form the complex with its oxygen-related groups and simultaneously grain the electrons from iron powder, which is finally induced to a dehydration process. Fig. 2b shows that the (001) diffraction peak of GO at ~11 °C disappears and the broad (002) diffraction peak of rGO at ~23 °C emerges. Additionally, the intensities of all C 1s peaks of carbon binding to oxygen significantly decrease accompanied with the reduction process as shown in Fig. 3b and c. The ratio of C 1s to O 1s peak areas in XPS spectra are used to calculate the atomic ratio of carbon and oxygen (C/O), describing the degree of GO reduction. With the reduction from GO to rGO, the C/O increases from 2.94 to 6.79, respectively. These results have suggested that partial oxygen-containing functional groups of GO is first effectively removed in the reduction reaction by iron powder and oxalic acid. Meanwhile, an aggregated phenomenon of rGO is also observed, which can be explained by the the electrostatic attraction between positive Fe^{2+}/Fe^{3+} ions and negative Fe-rGO sheets. Additionally, the impurity of Fe_3O_4 was also detected in the XRD and XPS patterns, which belongs to the adsorbed iron ions on the rGO surface.[47] Due to the separation of the adsorbed iron ions, it is effective to prevent the fresh rGO surface from restacking and make full use of the specific surface area of the unfold graphene. Meanwhile, the iron ions *in-situ* deposited on the rGO surface are regarded as the prior $LiFePO_4$ nuclei. With the addition of other raw sources of LFP and sugar added into the suspension, the obtained LFP nano-grains will be firmly adhered on the graphene sheets.

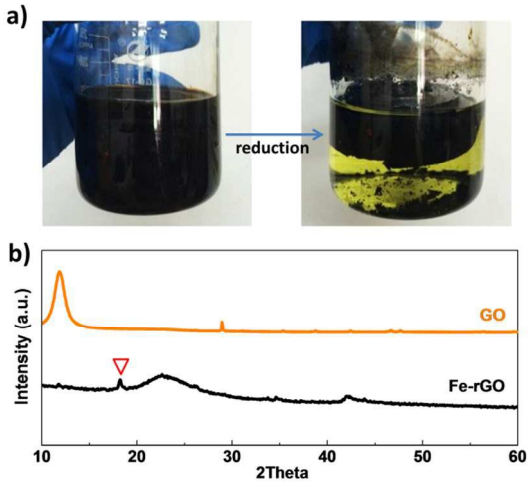

Fig. 2. (a) The visual change of the reaction mixture before and after the reduction reaction of GO. The image on the right shows the formation of black rGO. (b) XRD patterns of GO and Fe-rGO samples. Red inverted triangle represents Fe_3O_4 impurity adsorbed in the Fe-rGO surface.

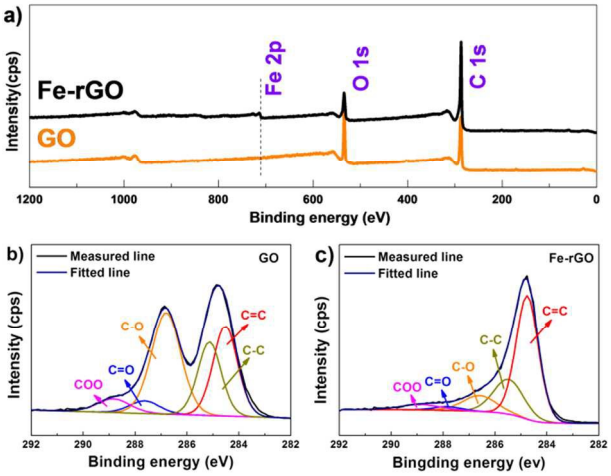

Fig. 3 XPS general spectra of GO and Fe-rGO samples (a), the curves fit of C 1s spectra of GO (b) and the curves fit of C 1s spectra of Fe-rGO (c).

XRD measurements are carried out to examine the crystal structure of LFP@C/Fe-rGO composite and confirm its well-crystallized orthorhombic structure $LiFePO_4$ phase with no diffraction peaks of impurities in Fig. 4a. Due to amorphous carbon coating and a low amount of graphene in the composites, there is only an observed broad diffraction peak of carbonaceous materials in this composite. The carbon content of the LFP@C/Fe-rGO composite is determined by TG in the air. Fig. S1 presents 93.7 wt.% residuals of the composite when the temperature increases to 800 °C. Meanwhile, there is ca. 5 wt.% mass increase of the total weight for LFP as the ferrous oxidation in high temperature.[48-50] Therefore, the calculated carbon content is 10.26 wt.%. SEM in Fig. 4b presents granular grains of *ca.* 100 nm with a trivial aggregation as well as a relative uniform distribution of particle size. Meanwhile, as shown in Fig. 4c, TEM manifests abundant carbon-coated $LiFePO_4$ grains are dispersed uniformly on a large unfolded graphene sheet. The small size of nanograins is effective to shorten the Li^+ diffusion distance in the crystals. [51] Compared with Fig. 4c and Fig. S2a,b, both LFP@C/Fe-rGO and LFP@C/GO have a uniform distribution of LFP grains on the graphene due to good dispersion of GO in the aqueous solution. But the slight aggregation of LFP@C/rGO is observed because of the hydrophobic feature of rGO after the thermal reduction. The high magnification TEM image shows a ~1 nm thickness of carbon coating on the surface of LFP particle. The carbon/graphene layered structure can improve the electronic conductivity and accommodate facile insertion and extraction of Li ions with the changing volume. [39] In addition, LFP@C/Fe-rGO nanocomposite has higher specific surface area of 54.78 m^2g^{-1} by BET surface area analysis, compared with the results in our previous work. [11, 39] The isotherms of the composite are type IV and belong to a Type H3 hysteresis loop, which typically indicates the existence of mesopores. [52] The inset in Fig. 5 presents that there are two different pore diameters existing in the composite, serving for the electrolyte infiltration and opening the pathways for ion transport. Good dispersion of $LiFePO_4$ particle on the unfold graphene in SEM observation is to achieve an enhanced specific surface area of the LFP@C/Fe-rGO nanocomposite, in favour of creating active sites for Li^+ insertion/extraction reaction.[15] This robust

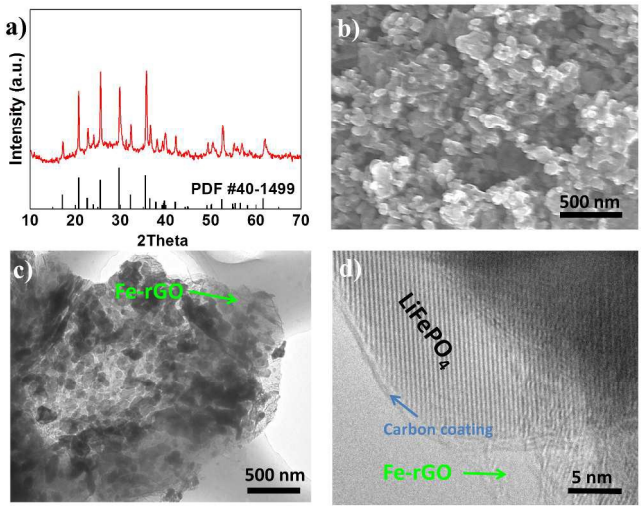

Fig. 4. XRD patterns (a); SEM (b) and TEM (c, d) of LFP@C/Fe-rGO nanocomposite.

structure makes the LFP@C/Fe-rGO nanocomposite possible to offer an excellent electrochemical performance.

The electrochemical properties of LFP@C/Fe-rGO electrode were evaluated by using a coin-type cell. After taking several cycles to stabilize cell capacity, Fig. 6a depicts a series of typical galvanostatic discharge/charge profiles of LFP@C/Fe-rGO at different rates. A flat charge plateau at ~ 3.45 V (*vs.* Li^+/Li) corresponds to the oxidation of Fe^{2+} to Fe^{3+} with the Li^+ moving toward the negative electrode and the discharge profile shows a planar platform at ~3.40 V associated with the reduction of Fe^{3+} to Fe^{2+} by the Li^+ insertion in LFP crystals. Their potential interval is only ~50 mV, implying an excellent reversibility and reactivity of LFP@C/Fe-rGO. In addition, the LFP@C/Fe-rGO electrode exhibits a specific discharge capacity of 154 mAh•g^{-1} at 0.2 *C* rate. With increasing current rates, specific discharge capacities of LFP/Fe-rGO at 1 *C*, 2 *C*, 5 *C*, 10 *C* and 20 *C* rate are up to 146.5, 142.1, 131.0, 119.9, and 107.3 mAh•g^{-1}, corresponding to *ca.* 95%, 92.2%, 85%, 77% and 69.7% of the value at 0.2 *C* rate, respectively, Meanwhile, the polarization values are increasing from ~100 to ~740 mV. In particular, the capacity of *ca.* 102 mAh•g^{-1} is charged within 100 seconds at 20 *C* rate through galvanostatic charge process, accounting for *ca.* 95% of the total capacity (107.3 mAh•g^{-1}) charged.

To highlight the outstanding properties of LFP@C/Fe-rGO, comparative samples of LFP@C/GO and LFP@C/T-rGO were synthesized. CV is first measured at 0.1 mV•s^{-1} in Fig. 6b, the typical redox peaks of the three samples are described, which corresponding to the Li^+ insertion/de-insertion in LFP crystals. LFP@C/Fe-rGO delivers the potential interval of 174 mV between a couple redox peaks, which is as expected the lowest value. Meanwhile, a higher peak current intensity of LFP@C/Fe-rGO also reflects a faster kinetics of electron and Li^+ transport, compared with that of LFP@C/GO and LFP@C/T-rGO. Rate capabilities of the three samples are given in Fig. 6c. At low current rates of less than 2 *C*, all the electrodes can deliver specific discharge capacities of over 135 mAh•g^{-1}, where their distinctions are not obvious. At more than 5 *C* rate, LFP@C/Fe-rGO electrode exhibits the best rate performance amongst three samples. LFP@C/Fe-rGO electrode delivers a high and stable

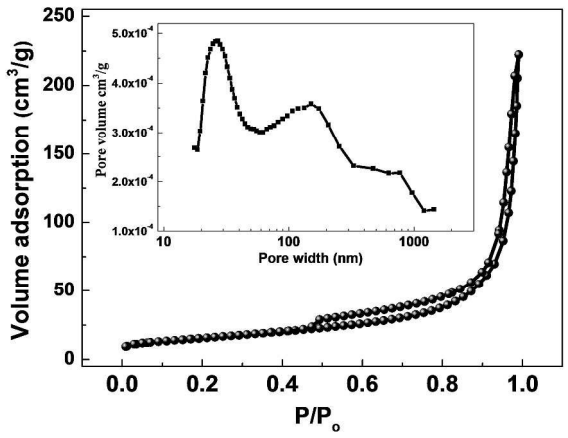

Fig. 5. Nitrogen isothermal-adsorption curves of the LFP@C/Fe-rGO nanocomposite. The inset: Pore size distribution in the LFP@C/Fe-rGO nanocomposite.

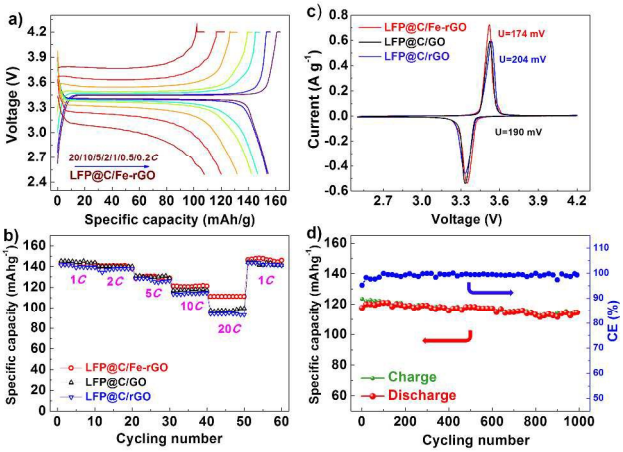

Fig. 6. Electrochemical properties: (a) Charge/discharge profiles of LFP@C/Fe-rGO at different rates; (b) CV curves of the three samples with the scanning speed at 0.1 mV·s^{-1}; (c) Rate capabilities of the three samples from 1 to 20 *C*; (d) Long cycling stabilities of LFP@C/Fe-rGO sample at 10 *C* rate.

specific capacity of 120 mAh•g^{-1}, while both LFP@C/GO and LFP@C/T-rGO only offer the specific discharge capacities of *ca.* 100 mAh•g^{-1}. It can be explained by uniform dispersion of active LFP nanograins on the high-conductive graphene sheets which support the feasibility of high-rate performance battery.

To verify the effect of the strong adhesion of LFP on the graphene on the cycling performance, a long cycling test was conducted at 10 *C* rate. After 1000 cycles of LFP@C/Fe-rGO electrode, its specific discharge capacity of 115 mAh•g^{-1} is still obtained in the last recorded cycle in Fig. 6d. The LFP@C/Fe-rGO nanocomposite only has a little decay on the specific discharge capacity with the capacity retention of *ca.* 95%, which is also better than our previous work. [39] The corresponding columbic efficiency is approaching 100% after the first few cycles. As known that graphene can buffer the frequent volume change from Li^+ insertion/extraction at high rate, the anchored $LiFePO_4$ grains cooperated with coating carbon are fixed firmly on crimp graphene surface, leading to the further reinforcement of the cycling performance.

On the basis of the above characterization results and

electrochemical investigations, the excellent performance of LFP@C/Fe-rGO nanocomposite comes from this specifically designed synthesis process, i.e., , dual functions of iron powder, acting as the green GO reductant and the raw source of $LiFePO_4$. This process also has a critical effect on the strong anchoring of LFP grains on the graphene sheets. During the reduced process of GO to rGO, the chemical reaction and electrostatic attraction promote the adsorption of the iron ions onto the rGO surface as the LFP nuclei. The uniform dispersion of anchored LFP grains makes full use of the specific surface area of exfoliated graphene sheets. The robust structure provides superior buffer capability to large volume change during high-rate charge/discharge process and effective permeation of electrolyte. Secondly, the dual reduction for graphene oxide is designed for the significant enhancement on the electric conductivity of graphene. The initial reduction from iron powder and oxalic acid can partially eliminate oxygen-containing functional groups on the surface of GO. Subsequently, the carbothermal process can further enhance complete removal of oxygen-containing functional groups on GO. Consequently, the electric conductivity of graphene is improved

Conclusions

In summary, a durable and cost-effective LFP@C/Fe-rGO cathode nanocomposite was successfully synthesized by using low-cost iron powder. The Iron powder plays the dual roles of the raw LFP source and the green GO reductant. With the reduction of GO to rGO by the iron powder, the produced iron ions are *in-situ* deposited on the rGO surface as the prior LFP nuclei. This will lead to the uniform distribution of carbon-coated LFP nanoparticles on the graphene sheets, which prevents the rGO from restacking large specific surface area and facilitate rapid electronic and ionic transport within the resultant composite. Additionally, it is worth noting that the chemical reaction contributes the enhanced electronic conductivity of the composite and facilitates the strong anchoring of the LFP nanoparticles onto graphene sheets. This robust structure therefore helps maintain the integrity of LFP@C/Fe-rGO nanocomposite in the rapid charge/discharge process. Finally, this strategy of using non-toxic and cheap iron powder may open up a new path for the development of other hybrid cathode materials with similar structures.

Notes and references

[a] *Harbin Institute of Technology, School of Chemical Engineering and Technology, Xidazhi Street, 150001 Harbin, China.Fax:86-451-86413721; Tel: 86-451-86413751; E-mail: wangdianlonghit@163.com*

[b] *Centre for Clean Environment and Energy, Environmental Futures Centre, and Griffith School of Environment, Gold Coast Campus, Griffith University QLD 4222, Australia. Tel: 61-7-5552 8155; E-mail: s.zhang@griffith.edu.au*

1. J. B. Goodenough and Y. Kim, *Chemistry of Materials*, 2009, **22**, 587.
2. V. Etacheri, R. Marom, R. Elazari, G. Salitra and D. Aurbach, *Energy & Environmental Science*, 2011, **4**, 3243.
3. L. Zhihua, Z. Duanming and Y. Fengxia, *J. Mater. Sci.*, 2009, **44**, 2435.
4. S. J. Gerssen-Gondelach and A. P. C. Faaij, *Journal of Power Sources*, 2012, **212**, 111.
5. A. K. Padhi, *Journal of the Electrochemical Society*, 1997, **144**, 1188.
6. B. L. Ellis, K. T. Lee and L. F. Nazar, *Chemistry of Materials*, 2010, **22**, 691.
7. J. W. Fergus, *Journal of Power Sources*, 2010, **195**, 939.
8. M. K. Devaraju and I. Honma, *Advanced Energy Materials*, 2012, **2**, 284.
9. L. X. Yuan, Z. H. Wang, W. X. Zhang, X. L. Hu, J. T. Chen, Y. H. Huang and J. B. Goodenough, *Energy & Environmental Science*, 2011, **4**, 269.
10. Y. Zhang, Q. Huo, P. Du, L. Wang, A. Zhang, Y. Song, Y. Lv and G. Li, *Synthetic Metals*, 2012, **162**, 1315.
11. T. Liu, L. Zhao, D. Wang, J. Zhu, B. Wang and C. Guo, *RSC Advances*, 2014, **4**, 10067.
12. C. Sun, S. Rajasekhara, J. B. Goodenough and F. Zhou, *J Am Chem Soc*, 2011, **133**, 2132.
13. G. Wang, H. Liu, J. Liu, S. Qiao, G. M. Lu, P. Munroe and H. Ahn, *Advanced Materials*, 2010, **22**, 4944.
14. Z. Bi, X. Zhang, W. He, D. Min and W. Zhang, *Rsc Advances*, 2013, **3**, 19744.
15. R. von Hagen, H. Lorrmann, K.-C. Möller and S. Mathur, *Advanced Energy Materials*, 2012, **2**, 553.
16. L. Dimesso, C. Forster, W. Jaegermann, J. P. Khanderi, H. Tempel, A. Popp, J. Engstler, J. J. Schneider, A. Sarapulova, D. Mikhailova, L. A. Schmitt, S. Oswald and H. Ehrenberg, *Chemical Society Reviews*, 2012, **41**, 5068.
17. H. C. Shin, K. W. Nam, W. Y. Chang, B. W. Cho, W.-S. Yoon, X.-Q. Yang and K. Y. Chung, *Electrochimica Acta*, 2011, **56**, 1182.
18. J. Wang and X. Sun, *Energy & Environmental Science*, 2012, **5**, 5163.
19. S. Li, J. Qiu, C. Lai, M. Ling, H. Zhao and S. Zhang, *Nano Energy*, 2015, **12**, 224.
20. C. Xu, B. Xu, Y. Gu, Z. Xiong, J. Sun and X. S. Zhao, *Energy & Environmental Science*, 2013, **6**, 1388.
21. G. Kucinskis, G. Bajars and J. Kleperis, *Journal of Power Sources*, 2013, **240**, 66.
22. H. Chang and H. Wu, *Energy & Environmental Science*, 2013, **6**, 3483.
23. H. Wu, Q. Liu and S. Guo, *Nano-Micro Letters*, 2014, **6**, 316.
24. S. Guo and S. Dong, *Chem Soc Rev*, 2011, **40**, 2644.
25. L. Peng, Y. Zhao, Y. Ding and G. Yu, *Chemical Communications*, 2014, **50**, 9569-9572.
26. L.-H. Hu, F.-Y. Wu, C.-T. Lin, A. N. Khlobystov and L.-J. Li, *Nature Communications*, 2013, **4**, 1687.
27. B. Wang, W. Al Abdulla, D. Wang and X. S. Zhao, *Energy & Environmental Science*, 2015, **8**, 869.
28. H. Ni, J. Liu and L.-Z. Fan, *Nanoscale*, 2013, **5**, 2164.
29. Z. Feng, C. Zhang, J. Chen, Y. Wang, X. Jin, R. Zhang and J. Hu, *Rsc Advances*, 2013, **3**, 4408.
30. L. Wang, L.-H. Tian, G.-D. Wei, F.-M. Gao, J.-J. Zheng and W.-Y. Yang, *Journal of Inorganic Materials*, 2011, **26**, 1009.
31. N. Recham, J. Oro-Sole, K. Djellab, M. R. Palacin, C. Masquelier and J. M. Tarascon, *Solid State Ionics*, 2012, **220**, 47.
32. K. Saravanan, P. Balaya, M. V. Reddy, B. V. R. Chowdari and J. J. Vittal, *Energy & Environmental Science*, 2010, **3**, 457.
33. Z. Chen, W. Ren, L. Gao, B. Liu, S. Pei and H. M. Cheng, *Nature Materials*, 2011, **10**, 424.
34. X.-m. Liu, P. Yan, Y.-Y. Xie, H. Yang, X.-d. Shen and Z.-F. Ma, *Chemical Communications*, 2013, **49**, 5396.
35. Z. Yanwu, M. Shanthi, C. Weiwei, L. Xuesong, S. J. Won, P. J. R. and R. R. S., *Advanced Materials*, 2010, **22**, 3906.
36. Z.-J. Fan, W. Kai, J. Yan, T. Wei, L.-J. Zhi, J. Feng, Y.-m. Ren, L.-P. Song and F. Wei, *ACS Nano*, 2010, **5**, 191.
37. C. K. Chua and M. Pumera, *Chemical Society Reviews*, 2014, **43**, 291.
38. C. Wang and J. Hong, *Electrochemical and solid-state letters*, 2007, **10**, A65.
39. B. Wang, D. Wang, Q. Wang, T. Liu, C. Guo and X. Zhao, *Journal of Materials Chemistry A*, 2013, **1**, 135.
40. Z.-S. Wu, W. Ren, L. Wen, L. Gao, J. Zhao, Z. Chen, G. Zhou, F. Li and H.-M. Cheng, *Acs Nano*, 2010, **4**, 3187.
41. S. M. Paek, E. J. Yoo and I. Honma, *Nano Letters*, 2009, **9**, 72.
42. J. Qiu, P. Zhang, M. Ling, S. Li, P. Liu, H. Zhao and S. Zhang,

ACS Applied Materials & Interfaces, 2012, **4**, 3636.
43. T. Wu, J. Gao, X. Xu, W. Wang, C. Gao and H. Qiu, *Nanotechnology*, 2013, **24**, 215604.
44. C. Hu, X. Zhai, L. Liu, Y. Zhao, L. Jiang and L. Qu, *Scientific Reports*, 2013, **3**, 2065.
45. Z. Xiong, L. L. Zhang, J. Ma and X. Zhao, *Chemical Communications*, 2010, **46**, 6099.
46. Z. Fan, K. Wang, T. Wei, J. Yan, L. Song and B. Shao, *Carbon*, 2010, **48**, 1686-1689.
47. P. Lian, X. Zhu, H. Xiang, Z. Li, W. Yang and H. Wang, *Electrochimica Acta*, 2010, **56**, 834.
48. Y. Shi, S.-L. Chou, J.-Z. Wang, D. Wexler, H.-J. Li, H.-K. Liu and Y. Wu, *Journal of Materials Chemistry*, 2012, **22**, 16465-16470.
49. I. Belharouak, C. Johnson and K. Amine, *Electrochemistry Communications*, 2005, **7**, 983-988.
50. J. Yang, J. Wang, D. Wang, X. Li, D. Geng, G. Liang, M. Gauthier, R. Li and X. Sun, *Journal of Power Sources*, 2012, **208**, 340-344.
51. B. Wang, B. Xu, T. Liu, P. Liu, C. Guo, S. Wang, Q. Wang, Z. Xiong, D. Wang and X. S. Zhao, *Nanoscale*, 2014, **6**, 986.
52. D. H. E. K. S. W. Sing, R. A. W. Haul, L. Moscou, R. A. Pierotti, J. Rouquérol and T. Siemieniewska, *Pure Appl. Chem*, 1985, 603.